Nitrogen plasma treatment of ZnO and TiO_2 nanowire arrays for polymer photovoltaic applications

Bello Ladan Muhammad[a,c], Franscious Cummings[b,*]

[a] Department of Physics and Astronomy, University of the Western Cape, Private Bag X17, Bellville 7535, South Africa
[b] Electron Microscope Unit, University of the Western Cape, Private Bag X17, Bellville 7535, South Africa
[c] Department of Physics, Ibrahim Badamasi Babagida University, P.M.B 11 Lapai, Niger State, Nigeria

ABSTRACT

This work reports on a simple, yet unique approach to improving the opto-electronic properties of vertically-aligned arrays of rutile TiO_2 and Wurzite ZnO nanowires by means of controlled nitrogen doping during exposure to highly kinetic radio-frequency generated N_2 plasma radicals. Morphologically, the plasma treatment causes a distortion of the vertical alignment of the nanowires due to a dissociation of the weak Van der Waals force clustering the nanowires. Optical spectroscopy show that plasma treatment increases the light transmission of TiO_2 arrays from 48% to 90%, with the ZnO arrays exhibiting an increase from 70% to 90% in the visible to UV range. The as-synthesized TiO_2 array has an indirect band gap of 3.13 eV, which reduces to 3.03 eV after N_2 treatment, with the ZnO equivalent decreasing from 3.20 to 3.17 eV post plasma exposure. A study of the 3d transition metal near edge fine structure of both Ti and Zn show that the N_2 plasma treatment of the nanowires results in nitrogen doping of both TiO_2 and ZnO lattices; this is confirmed by scanning transmission electron microscopy coupled with energy dispersive spectroscopy x-ray maps collected of single nanowires, which show a clear distribution of nitrogen throughout the metal-oxide. Application of these structures in P3HT:PCBM polymer blends shows progressive improvement in the photoluminescence quenching of the photoactive layer when incorporating both undoped and nitrogen-doped nanowires.

1. Introduction

An attractive approach to improve efficiency and reduce costs of modern hybrid photovoltaics such as polymer, perovskite and radial junction p-n type silicon cells, is the application of one-dimensional (1D) metal-oxides such as TiO_2 [1], ZnO as well as their nanocomposite forms [2–4]. The n-type nature of these materials has been widely exploited for use as an electron transport layer in these devices. However, this n-type character originates from the large density of oxygen vacancies generally detected on the surface of these 1D materials. In turn, these vacancies lead to electron trap-sites, causing electron–hole recombination during operation of the device. In addition, the presence of vacancies also changes the material's chemical reactivity and stability [5–9]. To overcome this constraint, nitrogen doping has been the preferred method, with various approaches employed, such as chemical doping during synthesis [10], high temperature annealing in a nitrogen ambient [11], ion implantation [12] and cathode magnetron sputtering [13]. Considering the above approaches, radio frequency (RF) plasma generation of highly reactive nitrogen species for substitutional

nitrogen doping in both TiO_2 [14] and ZnO [15], unlike chemical, in-situ or high temperature annealing approaches, allows for better control of the dopant flux, depth and concentration [16] by altering the plasma power, exposure time and temperature of the treated material. Dopants such as nitrogen and carbon generally serve as electron donors in metal-oxides [17–19], with the dopants introducing impurity states at various positions in the band gaps of both TiO_2 and ZnO, leading to different degrees of modification in electrical conductivity [20,21]; oxygen vacancies, on the other hand, are known to be shallow donors for TiO_2 and ZnO, with relatively low formation energies [22]. This study aims to contribute to this broad body of literature by showing that radiating TiO_2 and ZnO lattices with highly kinetic nitrogen plasma species has a unique, two-fold lattice effect: (1) passivation of the dangling Ti^{2+} and Zn^{2+} ionic species on the surface of the nanowire and (2) creation of deep-lying ionic bonds in the lattice leading to an increase in both electron conductivity and alteration of the optical behavior of the material. TiO_2 and ZnO NWs films are hydrothermally grown on fluorine-doped tin-oxide (FTO) substrates using well-known synthesis protocols [23,24], followed by plasma exposure for 10 min at

* Corresponding author.
  E-mail address: fcummings@uwc.ac.za (F. Cummings).

a N_2 plasma power of 500 W, while keeping the substrates at room temperature. The nitrogen modified nanowire/FTO substrates are subsequently used as electron transport layers to study the interfacial exciton dissociation in polymer photo-anodes with traditional poly(3-hexylthiophene)/6,6-phenyl C61-butyric acid methyl ester (P3HT/PCBM) blends used as the light absorber layer.

2. Experimental

2.1. TiO$_2$ and ZnO nanowire array synthesis

FTO coated soda lime glass substrates (F:SnO$_2$, MSE Supplies USA, 12–15 Ω per square) were initially cut into 2×1.5 cm^2 sizes, followed by successive ultrasonic bath cleaning in 2 vol% Hellmanex®-deionized water solution and 100% isopropanol for 5 min at 70 °C. The cleaned substrates were then dried in an argon stream and stored under vacuum until processing. During synthesis of the TiO$_2$ NWs arrays, a nutrient solution containing 12 ml of deionized water, 0.25 ml of tetrabutyl titanate and 10.5 ml of hydrochloride acid (37 wt%) was prepared and magnetically stirred for 10 min at ambient conditions. The solution was subsequently transferred to a Teflon liner and placed inside a high pressure reactive vessel (4744 General Purpose Acid Digestion Vessel 45 ml; Parr Instruments Company®), with the FTO substrates placed upright inside the liner during synthesis. A growth temperature and time of 150 °C and 4 h, respectively, yielded the most consistent nanowire structures and used as the optimum growth conditions. The lattice matching of the rutile F:SnO$_2$ substrate and rutile TiO$_2$ phase allows for the direct growth of the nanowires on the FTO substrates. However, for use as an ETL in organic-inorganic solar cells, a compact hole blocking layer directly grown atop the FTO layer is required [24] prior to nanowire synthesis. In this work this was achieved by spin-coating 35 μl of a solution comprising of 0.35 ml titanium isopropoxide dissolved in 5 ml ethanol, with 0.1 ml of 2 M hydrochloric acid (37 wt %) added as mediator. The final solution was stirred for 3 h at room temperature, then spin-coated for 30 s at 4000 rpm and sintered at 500 °C for one hour.

For ZnO NW array growth on FTO substrates, the lattice mismatch between the rutile FTO and stable hexagonal Wurzite phase of ZnO meant that a seed layer was first required on the FTO substrate. This seed layer also acted as hole blocking layer and consisted of a sol–gel solution, prepared using 0.7 M Zinc acetate dihydrate and 0.7 M ethanolamine in 25 ml ethanol and stirred for 10 min at room temperature, spin-coated at 3000 rpm for 40 s, followed by curing at 250 °C for 10 min to evaporate the solvent and improve ZnO particle adhesion to the substrate. The ZnO nanowires were then vertically grown by placing the seeded FTO/glass substrate upside down in the Teflon liner containing 25 mM zinc nitrate hexahydrate (Zn(NO$_3$)$_2$•6H$_2$O) and hexamethyleneteramine (HTMA) in 20 ml deionized water, which was mixed for 20 min at room temperature. Synthesis occurred at optimized temperature and time of 90 °C and 4 h, respectively. For both TiO$_2$ and ZnO structures, upon completion of the growth time, the autoclave vessels are removed from the oven and evaporatively cooled to room temperature before the removal of the substrate from the nutrient solution. This method allows for faster and more controlled ceasing of the nanowire growth. Once done, the samples were thoroughly washed in deionized water and dried under an argon stream followed by storing under vacuum for further processing.

2.2. Nitrogen plasma treatment and fabrication of glass/FTO/compact layer/nanowire/P3HT:PCBM photo-anodes

Fig. 1 shows a schematic representation of the experimental approach used to obtain N$_2$ plasma treated TiO$_2$ and ZnO NW arrays. The nanowire arrays were placed in a custom-built plasma-enhanced chemical vapor deposition chamber at a base and treatment pressure of 1.5×10^{-6} and 7×10^{-2} mbar, respectively. Prior to treatment, the plasma power was fine-tuned in a N$_2$:Ar gas mixture, controlled by keeping a constant gas flow rate of 100:100 sccm mixture. Based on previous optimization experiments, an optimum plasma power of 500 W (plasma power supply = 5 V; 1.25 A) yields the most consistent and significant changes in the opto-electronic behavior of both TiO$_2$ and ZnO structures. Once set, the Ar flow was reduced to 0 sccm, allowing for the red glowing N$_2$ plasma (see Fig. 1) to interact with the specimen; this point also signaled the time of exposure, set for a total of 10 min. Herein after the N$_2$ plasma treated TiO$_2$ and ZnO NW films will be referred to as N-TiO$_2$ and N-ZnO, respectively. A 30 μl drop of already prepared P3HT:PCBM 1:1 and 1:5 ratio solution was delivered onto the middle of the substrates of TiO$_2$ and ZnO NWs before and after N$_2$ treatment. The substrates were then spin-coated at 1000 rpm for 10 s, followed by 60 s at 2000 rpm. Firstly, the substrates were annealed at 90 °C for 30 min, cooled down for 10 min; annealed for the second time at 120 °C for 20 min, cooling down to room temperature and finally annealed at 150 °C for 20 min and allowed to cool down to room temperature before vacuum sealing for further analysis.

2.3. Characterization

The morphology of the nanowire films was characterized using a Zeiss Auriga field emission gun scanning electron microscope (FEG-SEM) operated at an accelerating voltage of 5 kV using an in-lens high resolution detector. The ZnO and TiO$_2$ nanowires samples for transmission electron microscopy (FEI Tecnai G^{2}20 FEG-TEM, 200 kV) imaging were detached from the FTO substrates, followed by dispersion in ethanol by sonication. A few drops of the sonicated suspension were drop-casted onto a holey carbon coated Cu copper grid, followed by drying under a high powered halogen lamp for 5 min. Energy dispersive x-ray (EDX) maps were collected of the P3HT:PCBM coated nanowires, whereas electron energy loss spectroscopy (EELS) was employed to quantify the nitrogen concentration in the individual nanowires. The x-ray maps were collected with the microscope operated in scanning transmission (STEM) mode, using a nominal probe size of 0.2 nm, at a camera length of 225 mm, which allowed for good x-ray counting statistics. All EDX data was collected using a liquid nitrogen cooled EDAX Si:Li detector, whereas all EELS spectra were obtained using a Gatan Image Filter (GIF-2001) operated in parallel beam mode. The drift-corrected EDX elemental maps collected in this study were obtained by scanning a 500×500 nm^2 grid on the sample, containing a few nanowires. Each grid comprised of 10×10 nm^2 pixels, with each pixel collected at a beam dwell time of 100 μs for a total spectral image (SI) collection time of approximately 17 min.

Grazing incidence x-ray diffraction (GIXRD) patterns were recorded using a PANalytical Empyrean diffractometer with CuKα radiation (λ = 1.5406 A$^\circ$) as x-ray source, operated at 45 kV, 40 mA. The incident beam was kept at 0.4° with respect to the substrate, with a 2θ range from 10 to 90° and 0.02° step size at 2 s per step for a total data acquisition time of 133 min. The incident beam optics comprised of a parabolic mirror, 4 mm mask, 1/16 divergence and 0.04 radians Soller slit, whereas the diffracted beam optics include a parallel plate collimator slit, 0.04 Soller collected by a PIXcel^{3D} 55 μm^2 (256×256 pixels) x-ray detector. To correct for the instrument broadening, a large area Si <100> substrate was used. Photoluminescence (PL) was employed to quantify the fluorescence from the samples of ZnO/NWs/P3HT: PCBM to determine if quenching exists between the donor and acceptor layers, using a Horiba NANOlog –TRIAX, USA spectrofluorometer with an excitation wavelength of 480 nm. UV–vis spectroscopy was performed to investigate the optical behavior of the as-synthesized and N$_2$ treated nanowires, using a Cecil UV–vis–NIR Spectrophotometer Unit 2021, operated between 200 and 900 nm.

3. Results and discussion

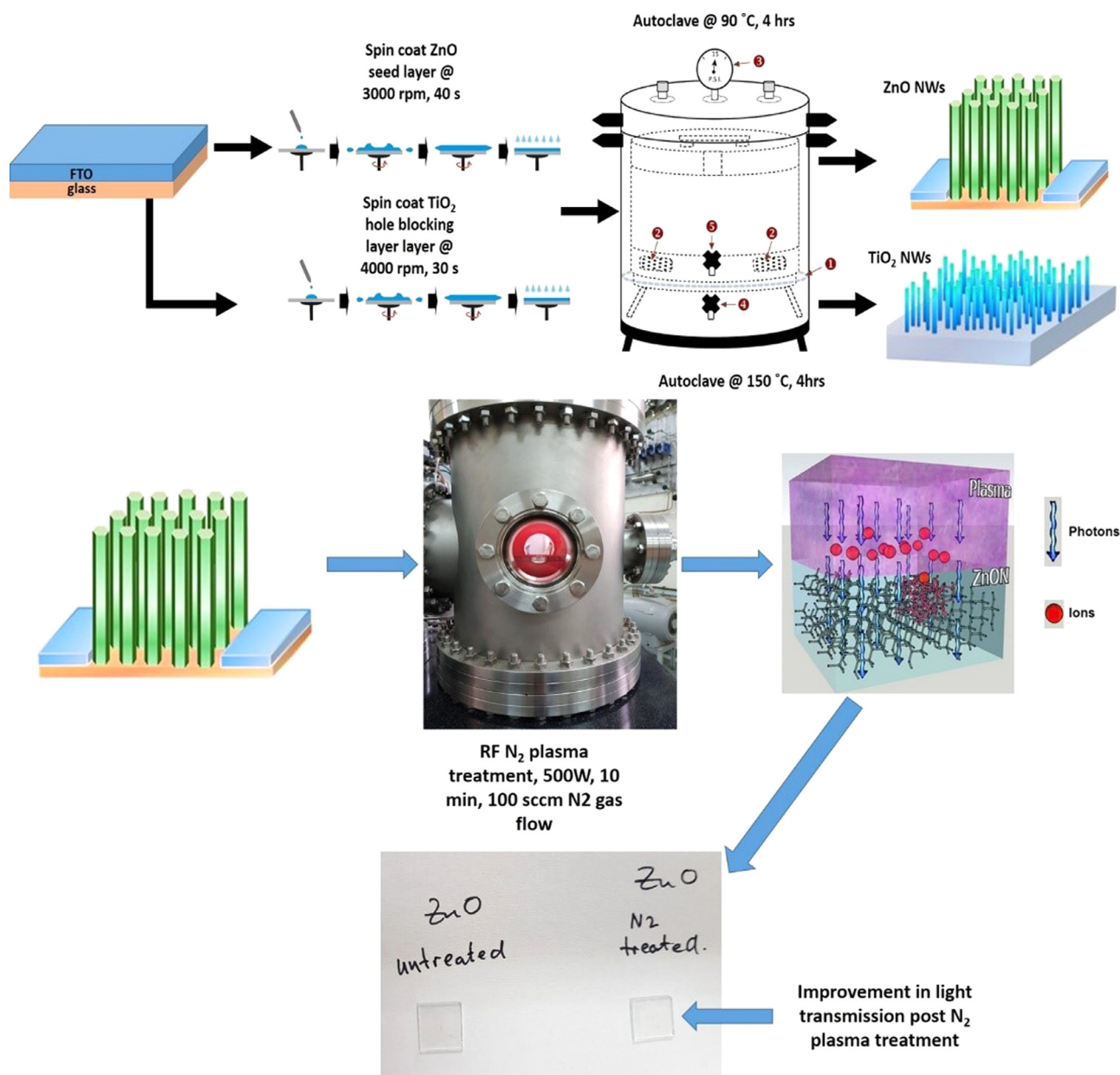Fig. 2 (a, c and b, d) show the micrographs of the top and cross-

Fig. 1. Schematic representation of the *(top row)* hydrothermal synthesis and; *(middle row)* N$_2$ plasma treatment; *(bottom row)* optical image of a glass/FTO/compact layer/ZnO NW array before and after N$_2$ treatment.
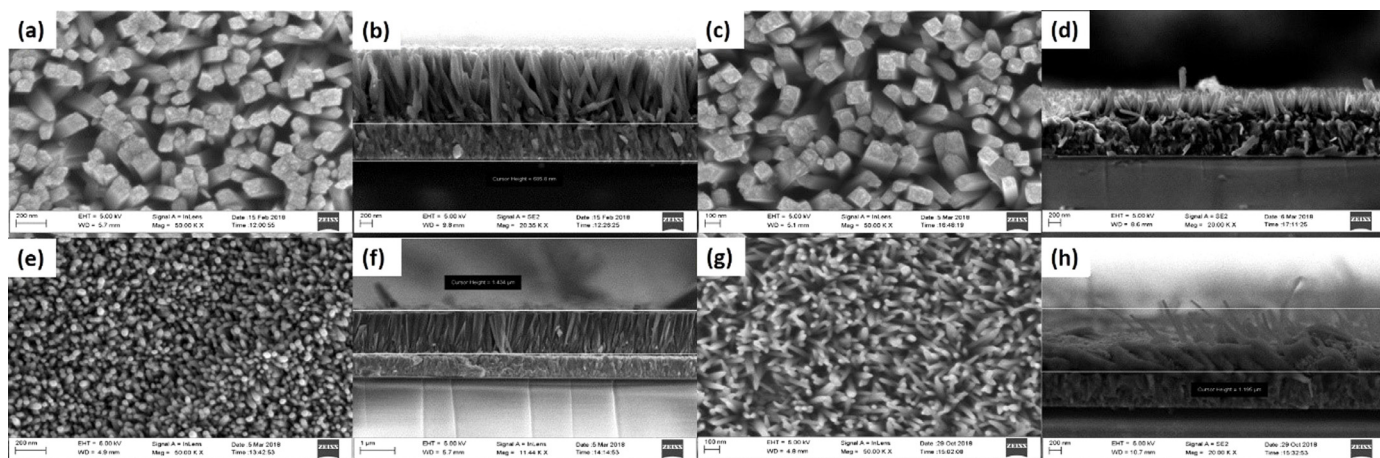

Fig. 2. Respective plan and cross-sectional SEM micrographs of (a, b) TiO$_2$; (c, d) N-TiO$_2$ (e, f) ZnO and (g, h) N-ZnO nanowires.

sectional views of the TiO$_2$ and N-TiO$_2$ NWs, respectively, whereas Fig. 2 (e, f and g, h) contain the micrographs of the top and cross-sectional views of the ZnO and N-ZnO NW films, respectively. These images clearly indicate that entire surface of the FTO substrates are covered uniformly and densely with vertically oriented TiO$_2$ and ZnO NWs. Furthermore, the TiO$_2$ NWs are tetragonal in shape with square top facets, which is the typical growth mechanism for tetragonal TiO$_2$ crystal structures [25]; the ZnO nanowires, in contrast, exhibit a needle-shape structure as discussed by Yhimura et al. [23] and Baruah et al. [26]. Moreover, it is also noticeable that the diameter of the ZnO NWs slightly increases after the plasma treatment while the vertical alignment of the nanowires, for both TiO$_2$ and ZnO become distorted, as can be seen from the cross-sectional images. The untreated TiO$_2$ NWs have an average diameter of 112.17 $\pm$ 29.3 nm and length of 1.391 $\pm$ 0.051 μm, while the N-TiO$_2$ nanowires have an average diameter of 110.9 $\pm$ 10.3 nm and length of 453.04 $\pm$ 49.2 nm. It must be noted that variance in length must be accounted for due to the error in measurement in establishing the perpendicular component in the SEM micrographs as well as the three dimensional non-alignment to the FTO substrate. The images of untreated ZnO NWs have an average diameter of 39.03 $\pm$ 6.31 nm and length is 1.33 $\pm$ 0.045 μm, with N-ZnO NWs having an average diameter of 48.47 $\pm$ 11.95 nm and length of 1.226 $\pm$ 0.142 μm. The SEM micrographs of the untreated ZnO NWs show an average diameter of 39.03 $\pm$ 6.31 nm and length of 1.33 $\pm$ 0.045 μm, with N-ZnO NWs having an average diameter of 48.47 $\pm$ 11.95 nm and length 1.226 $\pm$ 0.142 μm. The plan-view SEM images also show that N$_2$ plasma treatment decreases the areal density (i.e. number of nanowires per unit area) of the nanowires at their tops. This is due to dissociation of the weak, electrostatic Van der Waals forces bunching the nanowires at their apices. Furthermore, cross-sectional SEM micrographs show the nanowire orientation is distorted post N$_2$ treatment for both TiO$_2$ and ZnO structures; this is preferable for photovoltaic material deposition and improvement of the electron–hole dissociation interface during device operation [25,34].

Huang et al. [27] reported that an increase in nitrogen plasma treatment time of TiO$_2$ nanotubes leads to the decrease of surface area (length) and increases the pore diameter, which was attributed to the growth of TiO$_2$ crystallinities during sintering. Barakat et al. [28], on the other hand, performed a similar thermal-plasma treatment of TiO$_2$ and found that there was no significant change of surface area between the raw and treated samples at 400 °C for 60 min. A further study by Ishihara et al. [29] interestingly reported that N$_2$ plasma surface treatment was responsible for better photocurrent density of TiO$_2$ nanotube arrays for samples treated from 10 to 60 min. It was postulated that 10 min of plasma treatment was probably too brief to induce significant N-doping in the crystalline TiO$_2$ structures, whereas 60 min of treatment was found to be detrimental to the TiO$_2$ structure as a result of induced surface defects as compared to the 20-min treatments of the samples, which was found to be optimum. At any rate, all of the samples exposed to surface treatments (10, 20 and 60 min) had superior performance in comparison with the untreated samples. Annealing of TiO$_2$ nanotubes at the optimum temperature in the N$_2$ and O$_2$ atmospheres is also of critical importance in order to impart high electron conductivities which lead to high photocurrent densities. Several studies [e.g. 30] have shown that an annealing temperature in the range of 400–500 °C is most effective in transforming the amorphous phase of TiO$_2$ to crystalline anatase with a minimal fraction in the rutile form, whereas at higher temperatures, a more polycrystalline structure is formed with increasing amounts of rutile. These results show that nitrogen introduced in the TiO$_2$ lattice has a direct influence on both the crystallinity and electronic properties of the material, which in effect will influence the related optical properties. Similarly, it can be anticipated that the slight morphological changes of the TiO$_2$ NWs shown in Fig. 2(a)–(d) post N$_2$ plasma treatment, will have an influence on the optical properties of the material.

In the case of nitrogen plasma treated ZnO, Allami et al. [31]

reported the use of 100 W direct-current magnetron plasma and 450 V direct-current glow discharge plasma at different exposure periods of ZnO NWs and found that N incorporated in the ZnO lattice structure with multiple chemical states, including the well-screened molecular state (α-N$_2$), molecular nitrogen (γ-N$_2$) and α-N atoms occupying O sites to form Zn$_3$N$_2$ bonds. These results are in agreement with that reported by Tabet et al. [32], who added that ZnO$_{1-x}$N$_x$ forms by the decomposition of Zn$_3$N$_2$ and the re-arrangement of N atoms in the ZnO lattice [32] and NO$_2^-$ on the surface of ZnO thin films irradiated with nitrogen species during DC magnetron sputtering at low kV. Moreover, it was found that the chemical states and bonding energies of these vibrational states differ according to the plasma treatment type. In any ionizing environment, dissociation and recombination of the plasma species occur simultaneously, with the process that becomes prevalent depending on the plasma power [31]. This is particularly true in this study, as the high power radiofrequency plasma employed produces all three prevalent nitrogen species, namely α-N$_2$, γ-N$_2$ and atomic nitrogen. The α-N acts as an etching agent during treatment and causes the dissociation of the weak Van der Waals forces, as discussed above, leading to the disordering of the vertical alignment of both TiO$_2$ and ZnO nanowire arrays. The molecular nitrogen γ-N$_2$ in turn forms the Zn$_3$N$_2$ bond during substitutional doping of the ZnO lattice and decomposes into the ZnO$_{1-x}$N$_x$. Gao et al. [33] reported a change of growth direction of N-doped ZnO nanowires., whereas Yuan et al. [34] reported that N-doped ZnO nanowires grown at high temperature arrange along the [110] direction compared to the [001] direction for pure ZnO structures, which is ascribed to the difference in surface energy of the (100) and (110) plane densities, with the (110) facets more inclined to the incorporation of N atoms in the lattice, subsequently inhibiting the [001] growth of ZnO. Once more, as was the case for N-doped TiO$_2$, these studies show that the incorporation of N in the ZnO lattice causes a clear change in growth kinetics, which in turn will influence the measured crystalline and optical properties of the structures.

GIXRD patterns were collected to study the incorporation of the nitrogen in the metal-oxide lattices, the results of which are shown in Fig. 3. From the diffraction patterns it is found that the TiO$_2$ NWs grow in the tetragonal rutile phase and ZnO in the hexagonal Wurzite structure. Considering the geometry of the incident x-ray beam, i.e. parallel to the FTO/glass substrate and hence perpendicular to the growth of the nanowires, it can be seen that the TiO$_2$ nanowires grow predominantly along the rutile (101), whereas the ZnO stack along the (002) basal plane of the Wurzite hexagonal structure, along the length of the nanowires. From these patterns it is determined that the as-grown TiO$_2$ nanowire array has lattice constants $a = 0.467$ nm and $c = 0.292$ nm, which remain unchanged post N$_2$ plasma exposure.

The Williamson-Hall (W-H) transformation [35] of the GIXRD data, shown in Fig. 3(c) shows that the average crystalline grain size increases from 44 nm for the TiO$_2$ NWs to 60.79 nm for the N-TiO$_2$ NWs. At the incident x-ray beam angle of 0.4°, these grain sizes are comparable to the nanowire diameter, which was determined to be in the range of 100 nm from the SEM results of Fig. 2. The increase in nanowire diameter post N$_2$ plasma treatment is ascribed to an increase in the lattice strain, as shown by the W-H data of Fig. 3(c), due to the passivation of the dangling of Ti bonds deep in the TiO$_2$ matrix, caused by the reactive nitrogen species of the plasma during doping. In the case of ZnO an average crystalline grain size of 112.68 nm and lattice strain of 2.21×10^{-3} are calculated from Fig. 3(d) post plasma treatment compared to a grain size and strain of 76.57 nm and 1.58×10^{-3}, respectively for the as-synthesized nanowires. Once more the increase in diameter, caused by the increased lattice strain, is ascribed to the deep level doping of the ZnO lattice by the nitrogen during plasma exposure.

Fig. 4(a) and (b) shows UV–vis transmittance plots with a distinct improvement in light transmittance for both TiO$_2$ and ZnO NW arrays post N$_2$ plasma treatment. In particular, it can be seen that the TiO$_2$
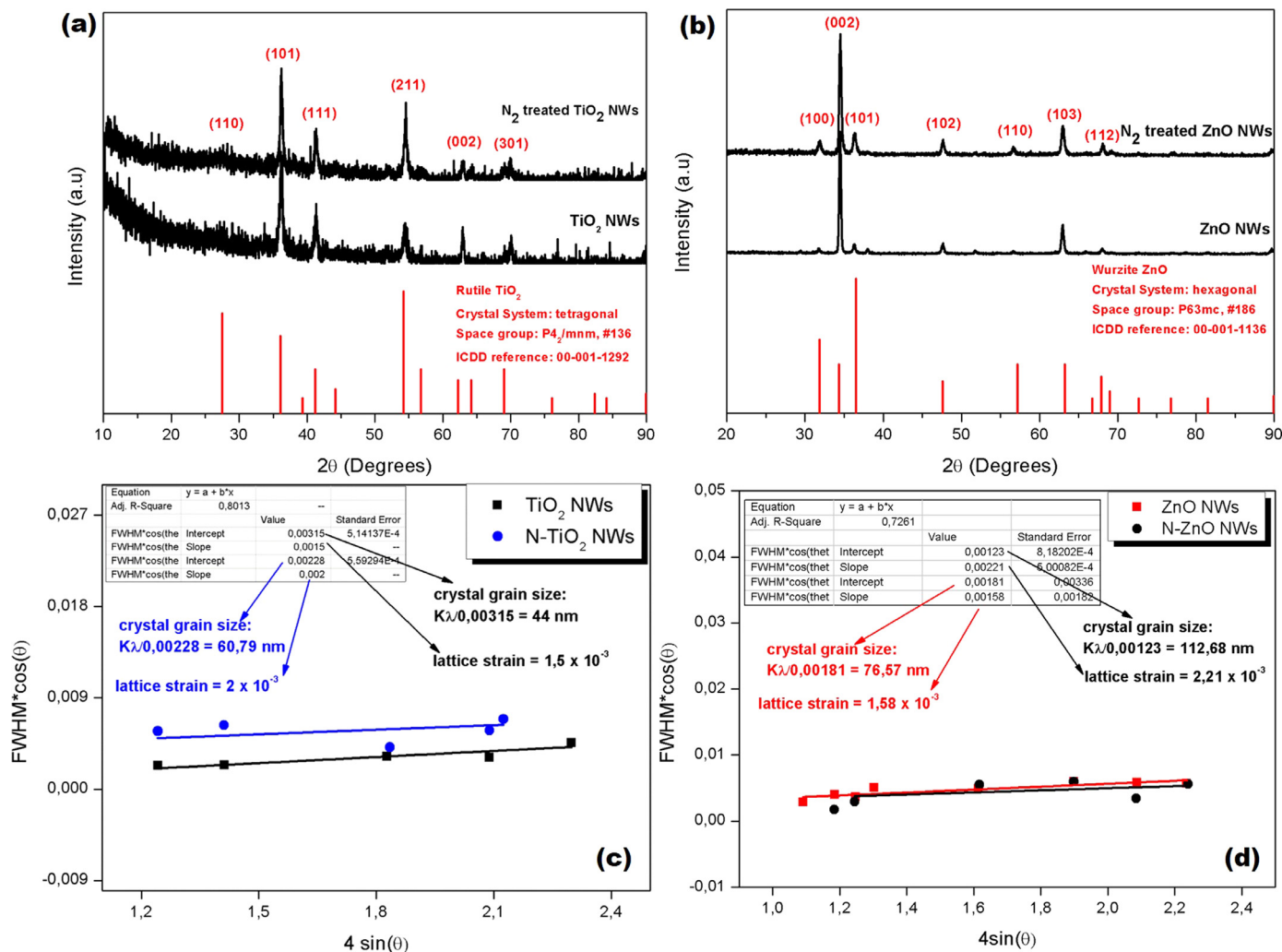
Fig. 3. GIXRD patterns of (a) TiO$_2$ and (b) ZnO NW arrays before and after N$_2$ plasma treatment; Williamson-Hall data of (c) TiO$_2$ and (d) ZnO NW arrays before and after N$_2$ plasma treatment.

array transmittance peaks at 90% at 750 nm after treatment compared to the as-synthesized structure with a low transmittance of 48% at the same wavelength. Similarly, the ZnO array transmittance increases from 70% to 90% over the same wavelength range, post plasma exposure. This is a significant result considering the fact that the metal-oxide nanowire films act as electron transport layers during solar cell operation and must not impede the light penetration (when illuminated from the FTO side) of the device. The improvement in transmittance is directly attributed to the distortion of the nanowire alignment by the N$_2$ plasma treatment, as shown in Fig. 2, caused by a dissociation of the electrostatic Van Der Waals force between two adjacent, vertically-aligned nanowires. The bandgaps of both TiO$_2$ and ZnO before and post plasma treatment were estimated using Tauc plots. To achieve this, $(\alpha h\upsilon)^{1/2}$ versus hυ was plotted, where ?? is the absorption coefficient and hυ is the photon energy. The absorption coefficient was calculated from the absorbance divided by the film thickness. The bandgap was estimated by extrapolating the linear portion of the Tauc plot of the x-axis, where value of $(\alpha h\upsilon)^{1/2}$ approaches zero. The respective Tauc plots for TiO$_2$ and ZnO are shown in Fig. 4(c) and (d).

The band gap obtained for TiO$_2$ NWs is 3.13 eV before and 3.03 eV after N$_2$ treatment, whereas the Tauc plot band gap of ZnO NWs is 3.20 eV before and 3.17 eV post treatment. The decrease in bandgap caused by an introduction of nitrogen in the TiO$_2$ lattice has been previously studied by Jinlong et al. [36], who reported that nitrogen doping leads to an increase in visible light absorption, which may be

attributed to the introduction of localized N 2p states, caused by atomic β-N, within the band gap. The reduction of the ZnO bandgap post N doping can similarly be explained by visiting previous literature. Reddy et al. [37] reported that extensive plasma exposures increase the amount of nitrogen implanted in ZnO nanorods, with the incorporation occurring in two ways, namely by interstitial and substitutional doping. During interstitial doping, the nitrogen atoms neutralize the defect states present on the surface of ZnO materials, whereas in substitutional doping, nitrogen impurities generate interstitial defects by replacing oxygen atoms. Khranovskyy et al. [38] report that, in general, the electrical conductivity of ZnO is primarily dominated by electrons generated from oxygen vacancies and zinc interstitial atoms. Various studies report that the conductivity of different types of semiconductors [39–42] reduces upon interstitial incorporation of nitrogen atoms in the lattice, diminishing the existing defect states due to passivation and subsequently minimizing the density of charge carriers. As such, the defects related absorption peak intensity strongly reduces in optical studies and may be accompanied by a decrease in band gap of ZnO since $E_g \propto n_i^{\frac{2}{3}}$, where n_i is the electron carrier density of an intrinsic semiconductor; this is also evident in Fig. 4(d). Extensive literature on the structural and optical effects of nitrogen plasma treatment on ZnO nanowire arrays are not readily available. Of the few studies published, Chantarat et al. [43], reported that nitrogen plasma treatment of both ZnO NWs and nanotubes causes insignificant structural damage in either structure, and noticed a reduction of the emission intensity of the
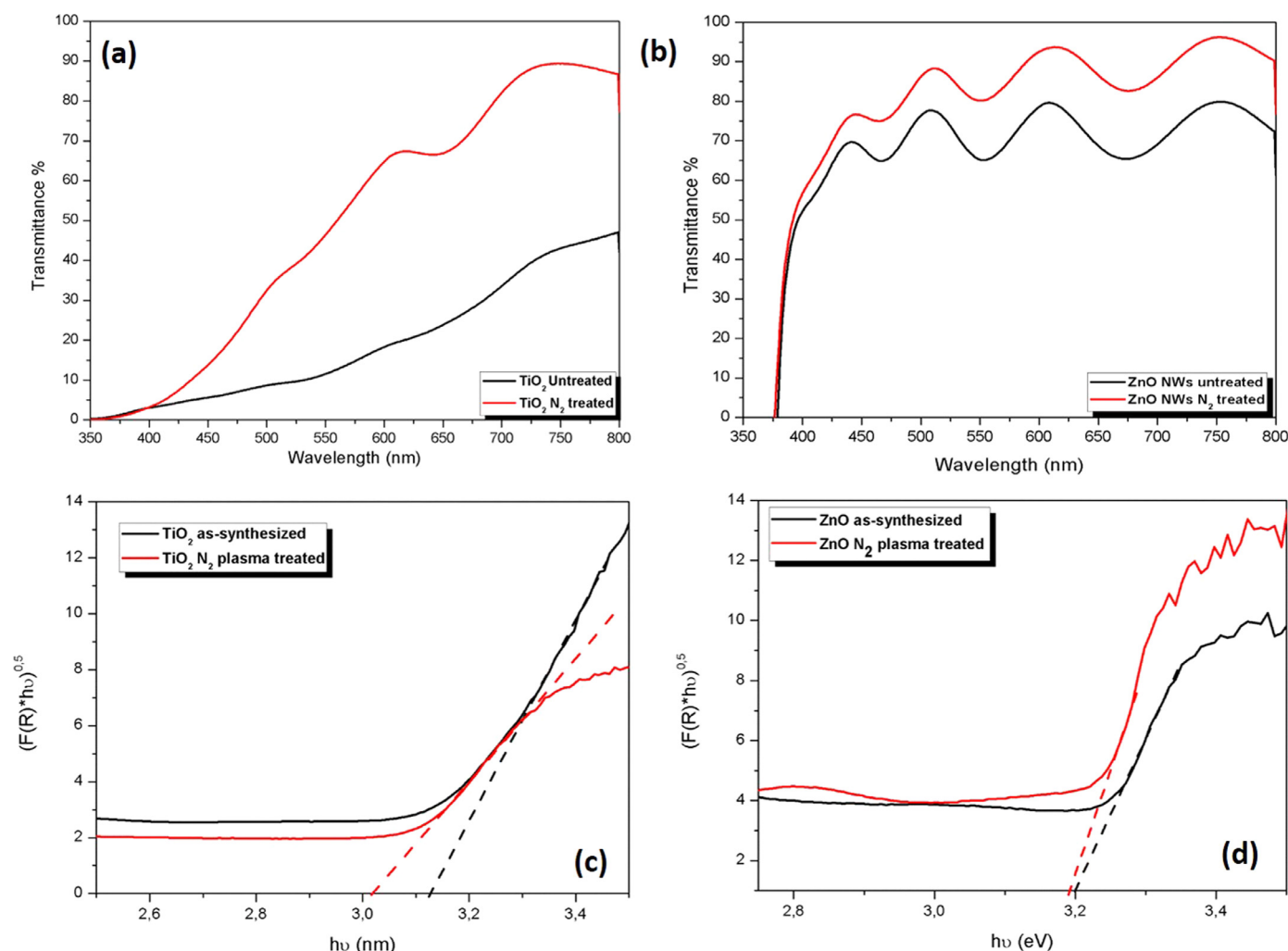
Fig. 4. UV–vis transmittance plots of untreated versus N_2 plasma treated (a) TiO_2 and (b) ZnO NWs films; Tauc plots comparing the untreated and N_2 plasma treated structures of (c) TiO_2 and (d) ZnO.

deep-level donor band; this was attributed to the passivation of the surface defects, mainly oxygen vacancies, of ZnO. Elsewhere, Lin et al. [44], reported that the broad emissions associated with intrinsic defects in ZnO NRs tend to disappear upon plasma treatment in NH_3 environments for 180 s, which indicates that the native defects or impurities contributing to visible transition can be greatly reduced by NH_3 plasma. However, it was observed that extensive plasma treatment can give rise to etching damage to the NR surface and results in the reduction of UV emission. These studies unanimously show that the nitrogen is introduced as a p-type dopant in the ZnO lattice during plasma treatment in a nitrogen rich environment. The dopants passivate the dangling Zn—O bonds that causes oxygen vacancies, thereby slightly reducing the electron charge transport in the structure. This is accompanied by a slight decrease in the optical bandgap, but more importantly a lowering of the conduction band minimum (E_c), which is especially important for heterojunction photovoltaic cell application, where any reduction in E_c is beneficial to the band alignment with the P3HT:PCBM blends. A final advantage of the nitrogen plasma treatment, as shown in the SEM micrographs of Fig. 2, extensive treatment leads to an etching effect, in accordance with [44], subsequently leading to lower areal density of NWs and improvement of light transmission through the nanowire array.

Fig. 5 (a, b) and (c, d) shows top and side-view SEM images of glass/FTO/ZnO NWs/P3HT:PCBM (1:1) and glass/FTO/N-ZnO NWs/P3HT:PCBM (1:1), respectively whereas Fig. 5 (e, f) and (g, h) shows

the SEM images of glass/FTO/TiO$_2$ NWs/P3HT:PCBM and glass/FTO/N-TiO$_2$ NWs/P3HT:PCBM (1:1), respectively. A clear distinction was observed between the untreated and treated samples of both TiO_2 and ZnO in that an increased contrast is observed as result of the N_2 treatment of P3HT:PCBM 1:1 sample on both ZnO and TiO_2 top images, as a result of the dissociation of the weak, electrostatic Van Der Waals forces on the areal density of NWs at the top, forming a less dense NW array. The cross-sectional SEM micrographs show the NW orientation is distorted after N_2 treatment for ZnO NWs, while the TiO_2 NWs remain vertically aligned to substrate, but with a lower areal density; both are recommended for photovoltaic material deposition.

HR-TEM, in combination with STEM, EDX and EELS were used to probe the internal structure, as well as the bonding and elemental concentration, as well as distribution of the N_2 treated TiO_2 and ZnO, as shown in Fig. 6. The analysis shows that each individual TiO_2 nanowire observed in the SEM consists of bundles of smaller nanowires (so-called fingers) having diameters ranging between of 10 and 20 nm; this is shown by the in-set of Fig. 6(a) and is consistent with the structures reported by Wisnet et al. [45]. In contrast, the ZnO structures primarily consist of a single structure, with a sharp, hexagonally-shaped tip, with a diameter range as determined from the SEM micrographs of Fig. 2; once more these are consistent with that reported previously [e.g. 46]. A study of the TiO_2 $L_{3,2}$ edge in the EELS spectra of Fig. 6(c) shows that the ratio of the L_3 (on the lower energy side of the spectrum) to L_2 (generally referred to as white-lines) changes upon the exposure of the
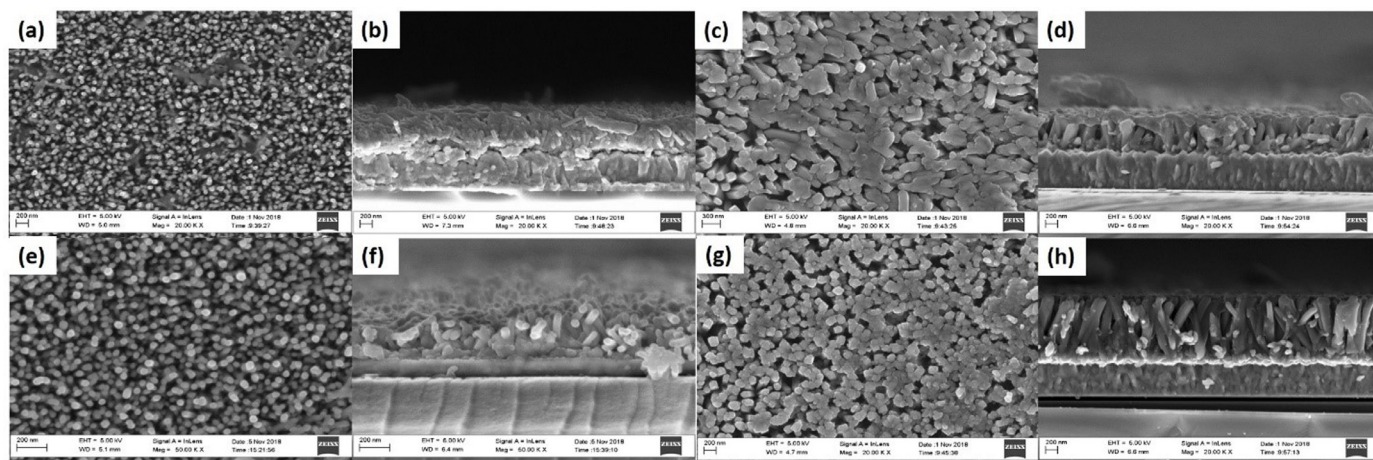
Fig. 5. Respective plan and cross-sectional SEM micrographs of P3HT:PCBM (1:1) spin-coated onto (a, b) TiO_2; (c, d) N-TiO_2 (e, f) ZnO and (g, h) N-ZnO nanowires.

nanowires to the N_2 plasma. At closer inspection, this change in ratio is found to be due to a change in the splitting of the L_3 and L_2 white-lines into respective t_{2g} and e_g sub-bands as a result of the common crystal field splitting associated with TiO_2 polymorphs [47,48]. From Fig. 6(c) it is found that the intensity ratio of the t_{2g} (on the low energy side of the respective L_3 and L_2 white-lines) to e_g sub-bands increases upon N_2 exposure for both the L_3 and L_2 peaks (red curve) as compared to as-synthesized TiO_2 structures (black curve). This change is indicative of the change in Ti-O $P4_2$/mnm space group symmetry of rutile caused by the introduction of N impurity atoms in the lattice of the metal-oxide. This change in lineshape, caused by the introduction of N, resembles that of other Ti_xO_y oxides, as reported previously [49]; in this case, however, the redistribution of the oxygen in the lattice by the N leads to the formation a Ti—N bond, thereby causing the change in symmetry. The STEM-coupled EDS spectral image (STEM-SI) collected of a single TiO_2 nanowire is shown in Fig. 6(g) and the extracted elemental maps of Ti, O and N shown in color; from these the distribution of nitrogen throughout the TiO_2 lattice is clearly observed (green color map).

In the case of the Zn $L_{3,2}$ of Fig. 6(f), the crystal field splitting leads to a sharp distinction of the L_3 and L_2 edges, post N_2 plasma treatment (red curve) compared to that found for the as-synthesized ZnO. The Zn $L_{3,2}$ edge characteristically does not split into distinct L_3 and L_2 white-lines, as in the case of TiO_2 [46,50], and as such the presence of the sharp L_2 line at 1043 eV, is very peculiar and once more evidence that the highly kinetic N infiltrates the ZnO lattice, causing a change in the local symmetry of the Zn metal by substitutional replacement of the oxygen in the lattice. Once more, the STEM-SI map of Fig. 6(h) shows the distribution of nitrogen (green map) throughout the ZnO lattice. Elemental quantification from EELS reveals that individual nanowires of TiO_2 are doped with 0.41 at% of N 100 atoms of Ti, O and N, equating to an atomic areal density of 1.86×10^{11} atoms/nm^2, whereas ZnO shows a N doping concentration of 0.62 at% N per 100 atoms of Zn, O and N or an areal density of 2.81×10^{11} atoms/nm^2. This result is in agreement with Koslowski et al. [51], who reported that although an incorporation of N cannot be ruled out completely due to the EELS detection limit of around 1%, the noticeable increase in electrical properties of ZnO thin films even at low nitrogen doping levels can only be ascribed to the incorporation of the N in the ZnO lattice.

Fig. 7(a) compares the PL of films of pure P3HT and P3HT:PCBM blended in 1:1 and 1:5 volume ratios, spin-coated on an FTO substrate, without the addition of an electron transport layer. As shown, in the absence of an ETL, minimal quenching of the main luminescence peak at ∼ 650 nm occurs. In contrast, in Fig. 7(b) an N-ZnO compact layer is added to the film arrangements of Fig. 7(a) and it becomes immediately clear that exciton dissociation occurs as evidenced by the quenching of the major PL peak. When two different materials are combined, i.e.

P3HT:PCBM [n-type, p-type] the intensity of the PL of the pristine materials (i.e. P3HT) drops abruptly, due to the quenching behavior of the blended mixture. This occurs due to electron transfer between the P3HT-donor and PCBM-acceptor. The drop in intensity may also be as a result of defect states present in the blended materials, which results in non-radiative recombination.

Good charge separation occurs as electrons generated in conduction band of P3HT donors are completely extracted by the acceptor PCBM, these in-turn increases the charge separation and quenching intensity [52]. Fig. 7(c) shows progressive improvement in the PL quenching of the photoactive layer, meaning the electrons and holes are effectively separated, as preferred for PV use. Similar behavior was found for N-TiO_2 films as well as for the as synthesized NW films (not shown in the manuscript for conciseness). The PL spectrum peaks reported are similar to the results reported in [52–55], while Omar et al. [56] reported that these peaks originate from recombination of electron–hole (e–h) pairs, localized within small sp^2 carbon clusters embedded within sp^3 matrix and agglomeration phenomena. The results of Fig. 7 show that the plasma treated layers are suitable for application in polymer solar cell devices.

4. Conclusions

In this study the optical properties of vertically-aligned arrays of rutile TiO_2 and Wurzite ZnO nanowires were modified by the introduction of N into the respective metal-oxide host lattices, during exposure to a radio-frequency generated nitrogen plasma at a high operating power. It was found that the nitrogen doping reduces the bandgaps of both TiO_2 and ZnO, as a result of the introduction of localized N 2p states close to the metal-oxide valence caused by a β-N bonding arrangement. Moreover, it was found that the changes are caused by N doping levels of less than 1 at% in individual TiO_2 and ZnO nanowires, which changes the crystal field splitting of both Ti $L_{3,2}$ and Zn $L_{3,2}$ edges as measured by EELS. Upon application of these structures in P3HT:PCBM polymer blends the photoluminescence quenching of the photoactive layer is significantly improved for both as-prepared and nitrogen-doped nanowires, thus making it an interesting and promising architecture for overall device efficiency improvement.

Declaration of Competing Interest

We wish to confirm that there are no known conflicts of interest associated with this publication and there has been no significant financial support for this work that could have influenced its outcome.
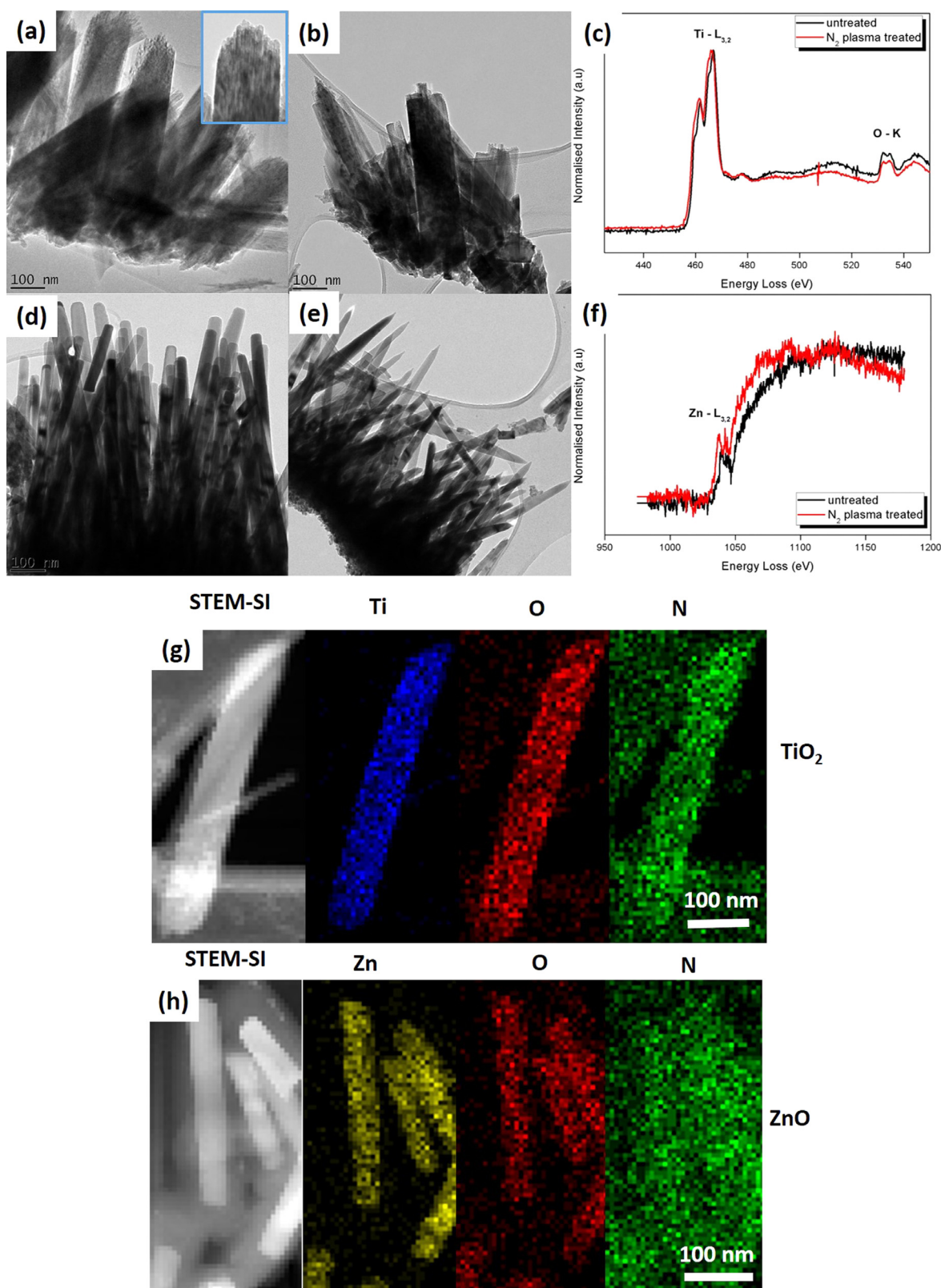
Fig. 6. (a, b) TEM micrographs of TiO_2 NWs and N-TiO_2 NWs, respectively; (c) electron energy loss spectra of Ti $L_{3,2}$ lineshapes before and after N_2 treatment; (d) STEM-EDS spectral image (SI) and respective elemental maps of an individual nitrogen doped TiO_2 nanowire (e, f) TEM micrographs of ZnO NWs and N-ZnO NWs, respectively; (g) EELS of Zn $L_{3,2}$ lineshapes before and after N_2 treatment; (h) STEM-SI and respective elemental maps of individual nitrogen doped ZnO nanowires.
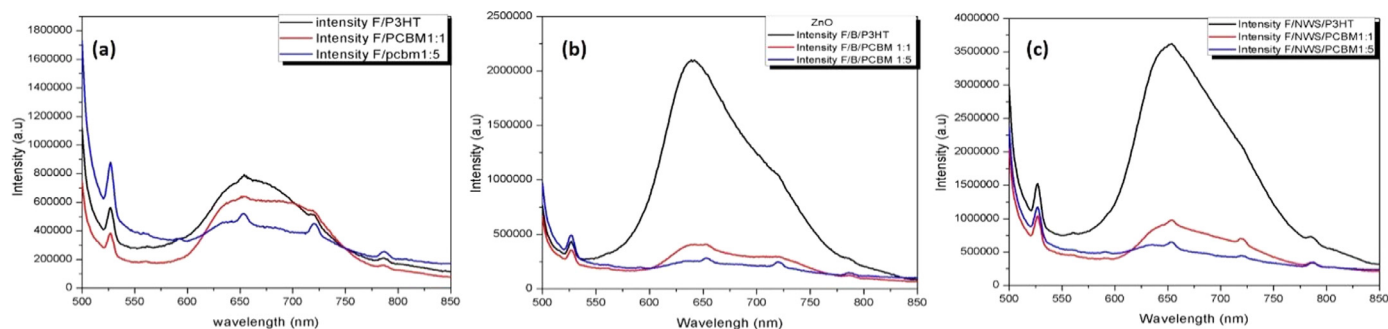
Acknowledgments

Fig. 7. PL comparing quenching behavior of the P3HT:PCBM blends (a) without an electron transport layer (ETL); (b) with the addition of a N-ZnO compact layer as an ETL; (c) ZnO NW array as an ETL.

References

[1] G.K. Mor, S. Kim, M. Paulose, O.K. Varghese, K. Shankar, J. Basham, C.A. Grimes, Visible to near-infrared light harvesting in TiO_2 nanotube array-P3HT based heterojunction solar cells, Nano Lett. 9 (2009) 4250–4257, https://doi.org/10.1021/nl9024853.

[2] J.H. Lee, J.H. Shin, Z.J.Y. Song, Y. Yi, Interface formation between tris(8-hydroxyqinoine) aluminum and nanowires and film, Appl. Phys. Lett. 97 (2010) 263302, , https://doi.org/10.1063/1.3531812.

[3] G. Williams, P.V. Kamat, Graphene-semiconductor nanocomposites, Excited-state interactions between ZnO nanoparticles and graphene oxide, Langmuir 25 (2009) 13869, https://doi.org/10.1021/la900905h.

[4] V. Alzari, V. Sanna, S. Biccai, T. Caruso, A. Politano, N. Scaramuzza, M. Sechi, D. Nuvoli, R. Sannaa, A. Mariani, Tailoring the physical properties of nanocomposite films by the insertion of graphene and other nanoparticles, Compos. Part B: Eng. 60 (2014) 29, https://doi.org/10.1016/j.compositesb.2013.12.011.

[5] G. Chiarello, V. Fabio, D.W. Boukhvalov, A. Politano, Sequestration of carbon monoxide at room temperature at vacancy sites of graphene, Chem. Commun 55 (2019) 8607–8610, https://doi.org/10.1039/C9CC04225C.

[6] A. Politano, G. Chiarello, R. Samnakay, G. Liu, B. Gürbulak, S. Duman, A.A. Balandin3, D.W. Boukhvalov, The influence of chemical reactivity of surface defects on ambient-stable INSE-based nanodevices, Nanoscale 8 (2016) 8474, https://doi.org/10.1039/C6NR01262K.

[7] A. Politano, M.S. Vitiello, L. Viti, D.W. Boukhvalov, G. Chiarello, The role of surface chemical reactivity in the stability of electronic nanodevices based on two-dimensional materials "beyond graphene" and topological insulators, FlatChem 1 (2017) 60–64, https://doi.org/10.1016/j.flatc.2016.11.003.

[8] A. Politano, G. Chiarello, C. Kuo, C.S. Lue, R. Edla, P. Torelli, V. Pellegrini, D.W. Boukhvalov, Tailoring the surface chemical reactivity of transition-metal dichalcogenide ptte2crystals, Adv. Funct. Mater. 28 (2018) 1706504, , https://doi.org/10.1002/adfm.201706504.

[9] Y. Liu, C.R. Gorla, S. Liang, N. Emanetoglu, Y. Lu, H. Shen, M. Wraback, Ultraviolet detectors based on epitaxial ZnO films grown by MOCVD, J. Electr. Mater. 29 (2000) 69, https://doi.org/10.1007/s11664-000-0097-1.

[10] X. Cheng, X. Yu, Z. Xing, J. Wan, Enhanced photocatalytic activity of nitrogen doped TiO_2 antase nanoparticle under simulated sunlight irradiation, Energy Procedia 16 (2012) 598–605, https://doi.org/10.1016/jegypro.2012.01.096.

[11] R. Rahimi, S.S. Moghaddam, M. Rabbani, Comparison of photocatalysis degradation of 4-nitrophenol using N,S co-doped TiO_2 nanoparticles synthesized by two different routes, J. Sol–Gel Sci. Technol. 64 (2012) 17–26, https://doi.org/10.1007/s10971-012-2823-6.

[12] H. Tsuchiya, J.M. Macak, A. Ghicov, P. Schmuki, Self-organization of anodic nanotubes on two size scales, Nano Lett. 7 (2006) 888–891, https://doi.org/10.1002/smll.200600035.

[13] K. Yamada, H. Yamane, S. Matsushima, H. Nakamura, T. Sonoda, S. Miura, K. Kumada, Photocatalytic activity of TiO_2 thin films doped with nitrogen using a cathodic magnetron plasma treatment, Thin Solid Films 516 (2008) 7560–7564, https://doi.org/10.1016/j.tsf.2008.05.048.

[14] J.B. Varley, A. Janotti, C.G. Van de Walle, Mechanism of visible-light photocatalysis in nitrogen-doped TiO_2, Adv. Mater. 23 (2011) 2343–2347, https://doi.org/10.1002/adma.201003603.

[15] X. Yang, A. Wolcott, G. Wang, A. Sobo, R.C. Fitzmorris, F. Qian, J.Z. Zhang, Y. Li, Nitrogen-doped ZnO nanowire arrays for photoelectrochemical water splitting, Nano Lett. 6 (2009) 2331–2336, https://doi.org/10.1021/nl/900772q.

[16] S.Z. Islam, A. Reed, N. Wanninayake, D.Y. Kim, S.E. Rankin, Remarkable enhancement of photocatalytic water oxidation in N_2/Ar plasma treated, mesoporous TiO_2 films, J. Phys. Chem. 26 (2016) 14069–14081, https://doi.org/10.1021/acs.jpcc.6b02622.

[17] J.H. Park, S. Kim, A.J. Bard, Novel carbon-doped TiO_2 nanotube arrays with high aspect ratios for efficient solar water splitting, Nano Lett. 1 (2006) 24–28, https://doi.org/10.1021/nl051807y.

[18] C. Burda, X.C. Y.Lou, A.C.S. Samia, J. Stout, J.L. Gole, Enhanced nitrogen doping in TiO_2 nanoparticles, Nano Lett. 3 (2003) 1049–1051, https://doi.org/10.1021/nl034332o.

[19] C.D. Valentin, G. Pacchioni, A. Selloni, Theory of carbon doping of titanium dioxide, Chem. Matter 26 (2005) 6656–6665, https://doi.org/10.1021/cm051921h.

[20] D.C. Cronemeyer, Infrared absorption of reduced rutile TiO_2 single crystals, Phys. Rev. 113 (1959) 1222.–11226, https://doi.org/10.1103/PhysRev.113.1222.

[21] F.F. Santiago, E.M. Barea, J. Bisquert, G.K. Mor, K. Shankar, C.A. Grimes, High carrier density and capacitance in TiO_2 nanotube arrays induced by electrochemical doping, Am. Chem. Soc. 34 (2008) 11312–11316, https://doi.org/10.1021/ja710899q.

[22] A. Janotti, J.B. Varly, P. Rinke, N. Umeazawa, G. Kresse, C.G. Van de Walle, Hybrid functional studies of the oxygen vacancy in TiO_2, Phys. Rev. B 81 (2010) 085212, , https://doi.org/10.1103/PhysRevB.81.085212.

[23] M. Yhimura, K. Byrappa, Hydrothermal processing of materials: past, present and future, J. Mater. Sci. 43 (2008), https://doi.org/10.1007/s10853-007-1853-x 2085-2013.

[24] X. Feng, K. Shankar, O.K. Varghese, M. Paulose, T.J. Latempa, C.A. Grime, Vertically aligned single crystal TiO_2 nanowire arrays grown directly on transparent conducting oxide coated glass: synthesis details and applications, Nano Lett. 8 (2008) 3781–3786, https://doi.org/10.1021/nl802096a.

[25] Z. Zhou, J. Fan, X. Wang, W. Zhou, Z. Du, S. Wu, Effect of highly ordered single-crystalline TiO_2 nanowire length on the photovoltaic performance of dye-sensitized solar cells, ACS Appl. Matter Interfaces 8 (2011) 4349–4353, https://doi.org/10.1021/am201001t.

[26] S. Baruah, J. Dutta, Hydrothermal growth of ZnO nanostructures, Sci. Technol. Adv. Mater. 10 (2009) 013001, , https://doi.org/10.1088/1468-6996/10/1/013001.

[27] C.M. Huang, L.C. Chen, K.W. Cheng, G.T. Pan, Effect of nitrogen plasma surface treatment to the enhancement of TiO_2 photocatalytic activity under visible light irradiation, J. Mol. Catal. A Chem. 261 (2007) 218–224, https://doi.org/10.1016/j.molcata.2006.08.020.

[28] M.A. Barakat, R. Kumar, Photocatalytic activity enhancement of titanium dioxide nanoparticles, Photocatalytic Activity Enhancement of Titanium Dioxide nanoparticles. Springer Briefs in Molecular Science, Springer, Cham, 2016, pp. 1–29 https://doi.org/10.1007.

[29] H. Ishihara, J.P. Bock, R. Sharma, F. Hardcastle, G.K. Kannarpady, M.K. Mazumder, A.S. Biris, Electrochemical synthesis of titania nanostructure arrays and their surface modification for enhanced photoelectrochemical hydrogen production, Chem. Phys. Lett. 489 (2010) 81–85, https://doi.org/10.1016/j.cplett.2010.02.038.

[30] N. Martin, C. Rousselot, D. Rondot, F. Palmino, R. Mercier, Microstructure modification of amorphous titanium oxide thin films during annealing treatment, Thin Solid Films 300 (1997) 113–121, https://doi.org/10.1016/S0040-6090(96)09510-7.

[31] S. Allami, Z.D.A. Ali, Y. Li, H. Hamody, B.H. Jawad, Liu L, T. li, Photoelectrochemical performance of N-doped ZnO branched nanowire photoanodes, Heliyon 3 (2017) e00423, https://doi.org/10.1016/j.heliyon.2017.e00423.

[32] N. Tabet, M. Faiz, A. Al-Oteibi, XPS study of nitrogen-implanted ZnO thin films obtained by DC-Magnetron reactive plasma, J. Electron. Spectrosc. Relat. Phenom. 163 (2008) 15–18, https://doi.org/10.1016/j.elspec.2007.11.003.

[33] J. Gao, X. Zhang, Y. Sun, Q. Zhao, D. Yu, Comensation mechanism in N-doped ZnO nanowires, Nanotechnology 21 (2010) 245703, , https://doi.org/10.1088/0957-4484/21/24/245703.

[34] G.D. Yuan, W.J. Zhang, J.S. Jie, X. Fan, J.A. Zapien, Y.H. Leung, L.B. Luo, P.F. Wang, C.S. Lee, S.T. Lee, P-type ZnO nanowire arrays, Nano Lett. 8 (2008) 2591–2597, https://doi.org/10.1021/nl073022t.

[35] V.D. Mote, Y. Purushotham, B.N. Dole, Williamson-Hall analysis in estimation of lattice strain in nanometer-sized ZnO particles, J. Theor. Appl. Phys. 6 (2012) 6, https://doi.org/10.1186/2251-7235-6-6.

[36] L. Jinlong, M. Xinxin, S. Mingren, X. Li, S. Zhenlun, Fabrication of nitrogen-doped mesoporous TiO_2 layer with higher visible photocatalytic activity by plasma-based ion implantation, Thin Solid Films 519 (2010) 101–105, https://doi.org/10.1016/j.tsf.2010.07.070.

[37] N.K. Reddy, M. Devika, Y. Hahn, Excellent enhancement in the device performance of nitrogen plasma treated ZnO nanorods based diodes, Nano Convergence Converg. 1(2014)26–31. 10.1186/s40580-014-0026-2.

[38] V. Khranovskyy, J. Eriksson, A. Lloyd-Spetz, R. Yakimova, L. Hultman, Effect of oxygen exposure on the electrical conductivity and gas sensitivity of nanostructured ZnO films, Thin Solid Films 517 (2009) 2073–2078, https://doi.org/10.1016/j.tsf.

2008.10.037.

[39] S.Y. Myong, K.S. Lim, Improvement of pin-type amorphous silicon solar cell performance by employing double silicon-carbide layer structure, J. Appl. Phys. 95 (2004) 1525–1530, https://doi.org/10.1063/1.1639140.

[40] T. Mattila, S.-.H. Wei, A. Zunger, Multiband coupling and electronic structure of (InAs)n/(GaSb)n superlattices, Phys. Rev. B 60 (1999) R11245, https://doi.org/10.1103/PhysRevB.60.5590.

[41] P.R.C. Kent, A. Zunger, Evolution of III-V nitride alloy electronic structure: the localized to delocalized transition, Phys. Rev. B 64 (2001) 115208, , https://doi.org/10.1103/PhysRevLett.86.2613.

[42] D.E. Aspnes, Third-derivative modulation spectroscopy with low-field electroreflectance, Surf. Sci. 37 (1978) 418, https://doi.org/10.1016/0039-6028(73)90337-3.

[43] N. Chantarat, Y. Chen, S. Chen, C. Lin, Enhanced uv photoresponse in nitrogen plasma ZnO nanotubes, Nanotechnology 20 (2009) 395201, , https://doi.org/10.1088/0957-4484/20/39/395201.

[44] C.C. Lin, H.P. Chen, S.Y. Chen, Synthesis and optoelectronic properties of arrayed p-type ZnO nanorods grown on ZnO film/Si wafer in aqueous solutions, Chem. Phys. Lett. 404 (2005) 30–34, https://doi.org/10.1016/j.cplett.2005.01.047.

[45] A. Wisnet, S.B. Betzler, R.V. Zucker, J.A. Dorman, P. Wagatha, S. Matich, et al., Model for hydrothermal growth of rutile wires and the associated development of defect structures, Cryst. Growth Des. 14 (2014) 4658–4663, https://doi.org/10.1021/cg500743u.

[46] Y. Ding, Z.L. Wang, Electron energy-loss spectroscopy study of ZnO nanobelts, J. Electron Microsc. 54 (2005) 287–291, https://doi.org/10.1093/jmicro/dfi039.

[47] R.D. Leapman, L.A. Grunes, P.L. Fejes, Study of the L23 edges in the 3d transition metals and their oxides by electron-energy-loss spectroscopy with comparisons to theory, Phys. Rev. B 26 (1982) 614–635, https://doi.org/10.1103/PhysRevB.26.614.

[48] R. Brydson, J.M. Thomas, Electron energy-loss spectroscopy (EELS) and the electronic structure of titanium dioxide, Solid State Commun. 64 (1987) 609–612,

[49] E. Stoyanov, F. Langenhorst, G. Steinle-Neumann, The effect of valence state and site geometry on Ti $L_{3,2}$ and O K electron energy-loss spectra of Ti_xO_y phases, American Mineralogist 92 (2007) 577–586, https://doi.org/10.2138/am.2007.2344.

[50] Z.H. Zhang, X.Y. Qi, J.K. Jian, X.F. Duan, Investigation on optical properties of ZnO nanowires by electron energy-loss spectroscopy, Micron 37 (2006) 229–233, https://doi.org/10.1016/j.micron.2005.10.016.

[51] U. Koslowski, K. Ellmer, P. Bogdanoff, T. Guminskaya, H. Tributsch, ZnO and TiO based nanostructres, J. Vac. Sci. Technol. A Vac. Surf. Films 24 (2006) 2199–2205 https://www.mdpi.com/journal/nanomaterials/special..issues/ ZnO.TiO$_2$nano.

[52] T.A. Chen, X. Wu, R.D. Rieke, Regiocontrolled synthesis of poly(3-alkylthiophenes) mediated by rieke zinc: their characterization and solid-state properties, J. Am. Chem. Soc. 117 (1995) 233–244 https://pubs.acs.org/sharingguidelines for options on how to legitimately share published articles.

[53] G. Janssen, A. Agurre, E. Goovaerts, P. Vanlaeke, J. Poortmans, J. Manca, Optimization of morphology of P3HT/PCBM films for organic solar cells: effects of thermal treatments and spin coating solvents, Eur. Phys. J. Appl. Phys. 37 (2007) 287–290, https://doi.org/10.1051/epjap:2007002.

[54] H. Wang, W. Hai-yu, B. Gao, L. Wang, Z. Yang, X. Du, Q. Chen, J. Song, H. Sun, Exciton diffusion and charge transfer dynamics in nano phase-separated P3HT/PCBM blend films, Nanoscale 3 (2011) 2280–2285, https://doi.org/10.1039/C0NR01002B.

[55] P. Jorge, D.E. Tieneke, B.A. Artem, V. Loosdrecht, H.M. Paul, K. Walter, T.M. Tuan, M. Juleon, D.A.L. Siebbeles, Photogeneration and ultrafast dynamics of excitons and charges in P3HT/PCBM blends, J. Phys. C 113 (2009) 14500–14506, https://doi.org/10.1021/jp904229q.

[56] B. Omar, P.M. Nametso, M. Khenfouch, A. Bokour, M. Baitoul, M. Maaza, J.W. Venturini, Photoluminescence quenching and structure of nanocomposite based on graphene oxide layers decorated with nanostructured porphyrin, Nanomater. Nanotechnol. 5 (2015) 71, https://doi.org/10.5772/60111.